



# Coupling hot isostatic pressing and laser powder bed fusion: A new strategy to manufacture defect-free CuCrZr-316L steel multi-material structures

## Journal Article

### Author(s):

Deillon, Léa; Abando Beldarrain, Nerea; [Li, Xiaoshuang](#) ; [Bambach, Markus](#) 

### Publication date:

2024-05

### Permanent link:

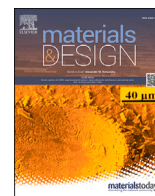
<https://doi.org/10.3929/ethz-b-000668716>

### Rights / license:

[Creative Commons Attribution 4.0 International](#)

### Originally published in:

Materials & Design 241, <https://doi.org/10.1016/j.matdes.2024.112914>



# Coupling hot isostatic pressing and laser powder bed fusion: A new strategy to manufacture defect-free CuCrZr-316L steel multi-material structures

L. Deillon<sup>a,\*</sup>, N. Abando Beldarrain<sup>b</sup>, X. Li<sup>c</sup>, M. Bambach<sup>a</sup>

<sup>a</sup> Advanced Manufacturing Laboratory, ETH Zurich, CH-8005 Zurich, Switzerland

<sup>b</sup> Laboratory for Nanometallurgy, ETH Zurich, CH-8093 Zurich, Switzerland

<sup>c</sup> Aerosint S.A., B-4040 Herstal, Belgium

## ARTICLE INFO

### Keywords:

Multi-material PBF-LB

Cu

Steel

Hot isostatic pressing

## ABSTRACT

Multi-material laser powder bed fusion (PBF-LB) offers new design opportunities by combining multiple materials into complex 3D shapes. However, for combinations with large differences in thermal, physical or elastic properties, avoiding interfacial defects is challenging. Combining Cu alloys with stainless steel is appealing for components necessitating high thermal / electrical conductivity in some areas and high strength and corrosion resistance in others. In this work, CuCrZr-316L samples were fabricated with a recoater allowing for deposition of two powders within a layer. As-printed samples exhibit significant intermixing and two types of defects: porosity in CuCrZr and steel cracking near the interface. Subsequent hot isostatic pressing (HIP) effectively addressed these issues by closing pores and healing cracks. Despite an overall softening, CuCrZr stays harder near the interface thanks to a very fine-grained structure retained after HIP. Alternatively, when CuCrZr powder near the interface is left unmelted and subsequently sintered, regions with small equiaxed grains and Cr-rich precipitates are formed, which exhibit properties similar to those of printed and HIPed CuCrZr. Hence, locally leaving powder unmelted and sintering it proved to be a successful strategy for producing defect-free 316L-CuCrZr components via PBF-LB, provided an airtight enclosure is ensured through proper design considerations.

## 1. Introduction

Laser powder bed fusion (PBF-LB) is one of the most technologically advanced additive manufacturing (AM) processes and has gained significant attention in various industries due to its ability to produce intricate designs with a high precision, and the potential to manufacture lightweight, high-performance parts. In contrast, multi-material PBF-LB (MM-PBF-LB) remains a largely unexplored field. MM-PBF-LB offers a remarkable wide range of new opportunities thanks to the possibility of combining two or more materials with significantly different properties (e.g., strength, corrosion resistance, thermal or electrical conductivity) into a complex 3D shape. MM-PBF-LB is gaining a rapidly growing attention, with first reviews on the topic recently published. These reviews agree that important technical barriers need to be overcome to bring MM-PBF-LB to an industrial level, such as the low level of manufacturing readiness of the pre-processing chain, the low recoating rates of MM-PBF-LB deposition setups, and the difficulty of recycling powder mixtures [1–4]. Among the technologies that enable MM-PBF-LB, the drum-based recoater system commercialized

by Aerosint SA enables the manufacturing of fully 3D multi-material structures with a sub-millimeter spatial resolution and relatively high recoating rates [2,5].

Besides the technical challenges, the development of MM-PBF-LB is also currently limited by the difficulty of achieving good bonding between the two deposited materials and defect-free interfaces, which may prove difficult for combinations of dissimilar metals which are prone to the formation of brittle intermetallic compounds or liquid metal embrittlement, and/or that exhibit large differences in coefficient of thermal expansion (CTE), laser absorptivity, melting temperature, thermal conductivity or elastic properties [1,3,6].

CuCrZr is a precipitation hardened alloy which, as such, offers an interesting combination of high electrical/thermal conductivity and mechanical strength, making it a good candidate for applications such as in the automotive, e-mobility and electrical industries. Combining the high thermal and electrical conductivity of copper alloys with the corrosion resistance of stainless steel would also benefit numerous industrial sectors, including e.g. the aerospace, marine and power industries. However, MM-PBF-LB of Cu alloys and stainless steel, similarly to laser

\* Corresponding author.

E-mail address: [ldellon@ethz.ch](mailto:ldellon@ethz.ch) (L. Deillon).

<https://doi.org/10.1016/j.matdes.2024.112914>

Received 22 January 2024; Received in revised form 19 March 2024; Accepted 3 April 2024

Available online 8 April 2024

0264-1275/© 2024 The Author(s). Published by Elsevier Ltd. This is an open access article under the CC BY license (<http://creativecommons.org/licenses/by/4.0/>).

**Table 1**  
Summary table of existing literature on MM-PBF-LB of Cu alloys and steels.

Materials	Geometry	Technique	Interface quality	Refs.
CuSn10-316L	2D, 3D	Ultrasonic deposition and suction module	Porosity, no cracking with Cu on top of steel and graded interfaces	[24–26]
CuCrZr-1.2709	2D, 3D	Ultrasonic deposition and suction module	Some cracks (only overview images of 3D samples), contamination	[23]
Cu-H13	2D, 3D	CNC machine with laser and powder hoppers	Good bonding for 2D interfaces (both sequences), 3D not characterized	[27]
CuCrZr-316L	3D	Aerosint recoater	No characterization	[28]
CuCrZr-316L	2D	Chamber opening	Cracks (Cu on top of steel)	[29]
CuCrZr-316L	2D	Chamber opening	Cracks (Cu on top of steel) that are minimized by the use of a ring-shaped beam	[30]
Cu18400-316L	2D	Recoater with separator	Cracks and pores (Cu on top of steel)	[31]
CuSn10-316L	2D	2 external hoppers	Cracks and pores (both printing sequences)	[22,32–35]
Cu52400-316L	2D	Chamber opening	Cracks and pores (both printing sequences)	[36]

welding of these two materials, is challenging due to the large mismatch in thermal conductivity between Cu and 316L steel ( $K_{Cu}/K_{316L} \approx 26$ ), and the high optical reflectivity of copper in the infrared wavelength. On a thermodynamic point of view, Cu and Fe show very limited mutual solubility and no intermediate compound under equilibrium conditions, but with high cooling rates such as those encountered in laser welding, the solubility of Cu in stainless steel can be as high as 20 to 22 at.% [7]. The Cu-Fe system is also known to show a metastable miscibility gap that leads to spinodal decomposition of the liquid, i.e., demixing of the liquid into a Cu-rich liquid and an Fe-rich liquid, at high cooling rates [8]. In addition, some steel grades, and in particular 316L, are sensitive to a specific type of liquid metal embrittlement known as copper contamination cracking (CCC), in which liquid Cu penetrates the grain boundaries of the steel and leads to intergranular cracking when high tensile stresses are present in the steel [9,10]. The mechanisms leading to CCC are not fully understood, but LME phenomena where failure occurs by wetting and penetration of grain boundaries tend to occur in systems showing low mutual solubility and a lack of intermetallic compounds, requirements that are both satisfied in the Fe-Cu system, as crack tip blunting is then limited [11,12]. The occurrence of CCC has been extensively reported in laser welding of Cu and steel [7,13–19], where strategies to achieve defect-free welds often consist in applying an offset of the laser beam toward the steel side and/or a beam angle that focuses most of the energy in the steel [20–22]. The addition of alloying elements to the Cu has also proven successful in suppressing or limiting the CCC of stainless steel during laser welding [16,19].

A few studies concern specifically MM-PBF-LB of different copper alloys and steels. These studies are summarized in Table 1 and can be separated according to whether 2D or 3D multi-material parts were manufactured, i.e., whether the material change occurred only along the build direction (2D) or also within a single printed layer (3D). Although some systems have been developed, mostly at a laboratory scale, to allow for the deposition of multiple powder materials in a single layer [5], 3D Cu-steel geometries have been only scarcely reported; those include squared core/shell structures [23], parts with a vertical “finger cross” interface [24], and a few more complex shapes [24–26].

Except in [24,25,33], a higher laser power is used for melting Cu. In samples built with an horizontal interface, this results in pronounced intermixing when Cu is melted on top of steel, with a thickness of the intermixing layer in the range 200–800  $\mu\text{m}$  [22,23,27,31–33,36]. With a vertical interface, the intermixing layer is even more extended and spans over 1 mm [27]. More porosity is commonly observed in Cu [24,25,27,31,36], whereas cracks are often found in the steel, close to the interface [22,23,27,29,31–33,36]. Cracking is indeed likely to oc-

cur due to the build-up of high residual tensile stresses, which arises from CTE and thermal conductivity mismatch, and the CCC sensitivity. Furthermore, Mao et al. investigated the influence of different parameters on the integrity of parts produced with CuCrZr on top of 316L and found that cracking in the steel can be limited by decreasing the scanning speed, increasing the hatching distance and increasing the power used to melt CuCrZr [29]. The EBSD investigations conducted by [31], [37] and [32] also revealed the presence of very fine (<1  $\mu\text{m}$ ) grains in interfacial areas of 316L/C18400, Maraging steel/T2 Cu alloy and 316L/CuSn10 bi-metallic parts, respectively.

In summary, despite great technological importance, no approach has yet been developed to reliably produce defect-free CuCrZr-316L components by MM-PBF-LB, especially when CuCrZr is added on top of 316L and when geometries with vertical interfaces are produced. Therefore, there is an undeniable need to develop alternative methods to conventional MM-PBF-LB, in order to fully exploit the potential offered by the possibility of combining these two dissimilar materials into a single component of complex geometry. In this study, we aim to explore the potential of combining MM-PBF-LB with a subsequent hot isostatic pressing (HIP) treatment, in order to develop innovative strategies for improving the integrity and functionality of dissimilar material combinations for technological applications. In particular, the effect of the post-PBF-LB HIP treatment on the microstructure, integrity and local mechanical properties of the interface is characterized and discussed.

## 2. Materials and methods

The starting raw materials are spherical 316L stainless steel powder from Carpenter Additive<sup>®</sup> ( $d_{10} = 19.9 \mu\text{m}$ ,  $d_{50} = 31.5 \mu\text{m}$ ,  $d_{90} = 49.5 \mu\text{m}$ ) and CuCrZr alloy from ECKART TLS ( $d_{10} = 7.19 \mu\text{m}$ ,  $d_{50} = 17.44 \mu\text{m}$ ,  $d_{90} = 26.61 \mu\text{m}$ ), both produced via gas atomization. The chemical composition of the powders, as provided by the manufacturers, is given in Table 2. The bi-metallic parts were built by PBF-LB using an Aconity Midi+ equipped with an infrared fiber laser ( $\lambda = 1070 \text{ nm}$ ) in combination with a newly developed recoater from Aerosint SA. The dual-material recoating unit, schematically represented in Fig. 1, comprises two rotating drums, one for each material, on which a thin layer of powder is first deposited and maintained at the surface of a mesh by a slight underpressure, before being locally ejected by pressurized gas. The height of the powder bed thus obtained is finally adjusted to the desired height by a metallic blade. The recoater allows for deposition of dual-material patterns with an in-plane resolution of  $500 \times 500 \mu\text{m}$ .

All structures were built onto a 316L base plate without preheating, under a protective Ar atmosphere, with a rotation of  $90^\circ$  between

**Table 2**  
Chemical composition of the powder materials, in wt.%.

Material	C	Cr	Ni	Mo	Mn	Si	Fe	S	Cu	Zr
316L	0.02	17.7	12.6	2.36	0.77	0.66	Bal.	0.006	-	-
CuCrZr	-	1.05	-	-	-	<0.004	0.02	-	Bal.	0.12

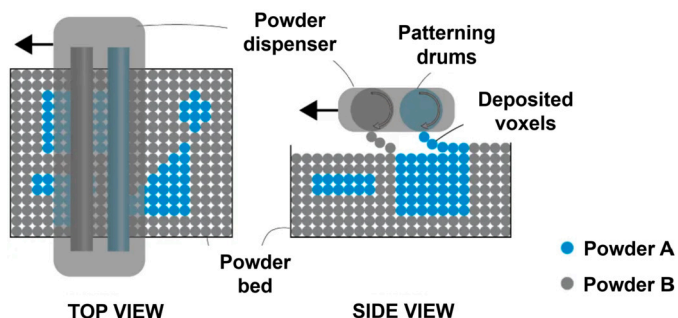


**Fig. 1.** Schematic of the dual-material recoater (adapted from Aerosint S.A.).

successive layers, a bi-directional meander scanning strategy, a layer thickness of 40  $\mu\text{m}$  and a laser beam diameter of 80  $\mu\text{m}$ . Steel was scanned with a laser power of 150 W, a speed of 600 mm/s and a hatch spacing of 80  $\mu\text{m}$ . A power of 500 W, a speed of 550 mm/s and a hatch spacing of 120  $\mu\text{m}$  were used to melt the CuCrZr twice, with a 90° rotation between the first and the second melting steps. For both materials, the laser power and speed values were selected based on the results of a parameter optimization study, which showed that these specific parameters maximize the density of the parts produced. For vertical interfaces, 316L was scanned before CuCrZr, without any overlap of the scanning vectors.

The sample geometry, depicted in Fig. 2, consists of 4 × 4 × 4 mm CuCrZr cubes centered within 10 × 10 × 10 mm 316L cubes. In some of those samples, a 100  $\mu\text{m}$ -thick layer of CuCrZr powder was left unmelted at the vertical interfaces with 316L, the thickness of the gap being defined as the distance between scan vectors.

The post-PBF-LB hot isostatic pressing (HIP) treatment was performed in a QIH15L furnace (Quintus Technologies AB) at 1055 °C for 5 h with an Ar pressure of 207 MPa on fully melted and partially melted samples. Parameters were chosen such as to maximize HIP efficiency, i.e., the pressure was set to the maximum achievable pressure of the equipment used, the temperature was set close to the melting point of CuCrZr (1070-1080 °C), and time was chosen such as to allow for atomic diffusion over a significant distance. The isothermal holding was followed by a fast cooling down to room temperature (approximately 14 minutes).

Cross-sections of the samples were cut, hot-embedded in conductive resin, ground with SiC papers and polished down to 0.04  $\mu\text{m}$  silica suspension for scanning electron microscopy (SEM) observations, which were conducted on a Zeiss EVO10 microscope equipped with an X-max detector (Oxford Instruments) for chemical analyses by energy dispersive X-ray (EDX) spectroscopy. Imaging and EDX analyses were done at an accelerating voltage of 15 kV and a current of 500 pA. Electron back-scattered diffraction (EBSD) analyses were carried out with a Hitachi SU5000 microscope equipped with EDX (Ultim Max, Oxford Instruments) and EBSD (Symmetry S3, Oxford Instruments) detectors. Data were acquired at 20 kV, 21 nA, with a 70° tilt angle and a 1  $\mu\text{m}$  step size. Because the Fe and Cu FCC phases have very close cell parameters (0.366 and 0.361 nm, respectively), EDX and EBSD signals were coupled to be able to distinguish between them. Post-processing was performed with the software AztecCrystal to remove wild spikes. Note that all close-up micrographs, EDX and EBSD analyses of vertical interfaces were acquired at approximately mid-height of the samples.

An iNano nanonindenter (Nanomechanics, Inc) was used to acquire hardness and reduced modulus mappings of interfacial areas. Measure-

ments were done in the NanoBlitz 3D mode with a diamond Berkovich indenter. The maps were performed in load control to an applied load of 2 mN and a spacing of 2  $\mu\text{m}$ . The target load was optimized with the Continuous Stiffness Measurement (CSM) mode for the desired mapping resolution in Cu, the softer phase, in order to avoid overlapping effects. Two adjacent 200x75 grids of indentations were performed covering 800  $\mu\text{m}$  in length and 150  $\mu\text{m}$  in width. However, the size of the grid was limited by cracks in the sample that did not undergo HIP post-processing, for which the grid length was reduced. As silica particles tend to become embedded in the samples surface during the final polishing step, the samples were re-polished with a 0.25  $\mu\text{m}$  diamond suspension prior to nanoindentation measurements. Data were evaluated by the standard Oliver and Pharr method.

### 3. Results

#### 3.1. As-printed microstructure

SEM micrographs giving an overview of the microstructure and defects present in an as-printed CuCrZr-316L cube are presented in Fig. 3. In all micrographs shown in this section, the build direction is oriented upwards with respect to the page. In addition, all SEM micrographs were taken with a BSE detector, whose contrast is such that brightness increases with atomic number and thus CuCrZr appears brighter than 316L.

With regard to defects, rather large irregular pores can be observed in CuCrZr, especially close to the vertical and bottom (i.e., CuCrZr on 316L, visible in the right image) interfaces. Numerous cracks can also be observed in the steel, especially near the vertical interface with CuCrZr but also at proximity with the bottom interface. Comparing the left and right images of Fig. 3, there is obviously significantly more intermixing when CuCrZr is melted on steel (right image) compared to the case when steel is melted on top of CuCrZr (left image), due to the large energy input needed to melt the Cu. In the latter case, the microstructure suggests that CuCrZr is significantly remelted only upon addition of the first 1-2 layers of steel (rotated by 90° from each other). On the other hand, at the CuCrZr on steel interface, considerable intermixing is visible over a thickness of more than 400  $\mu\text{m}$ , i.e., more than 10 layers.

At vertical interfaces, strong thermal and solutal Marangoni convection flows give rise to a very pronounced intermixing, with Cu being visibly dragged sometimes over more than 300  $\mu\text{m}$  into the steel, see e.g. where the yellow arrow at the bottom of the left image in Fig. 3 points. These extended Cu-rich channels are not observed at a frequency corresponding to each individual printed layer. Also, if Cu were drawn into the steel only when a scan track of the steel that is directly adjacent to CuCrZr and parallel to the interface is lased, then this would be over a distance less than 300  $\mu\text{m}$  (melt pool width is of the order of 85-130  $\mu\text{m}$ ). These channels thus occur more likely when the laser scans the interface with a direction perpendicular to it, as scan vectors do not end exactly at the interface, as evidenced later in Section 3.2.

The EDX results presented in Fig. 4 show that in the vertical configuration, the total intermixing area, which is indicated by the blue rectangular frame on the composition profile, is approximately 600  $\mu\text{m}$  thick. The EDX line profile also shows that the Cu (and O) content in the steel tends to be higher close to cracks, as highlighted by the red dashed lines and peaks encircled in Fig. 4. Note that the leftmost Cu peak in the steel is not associated with any visible crack, but given the interaction volume of EDX analyses (approximately 1  $\mu\text{m}$  deep), it can be assumed that the crack which is visible above the yellow line, to the

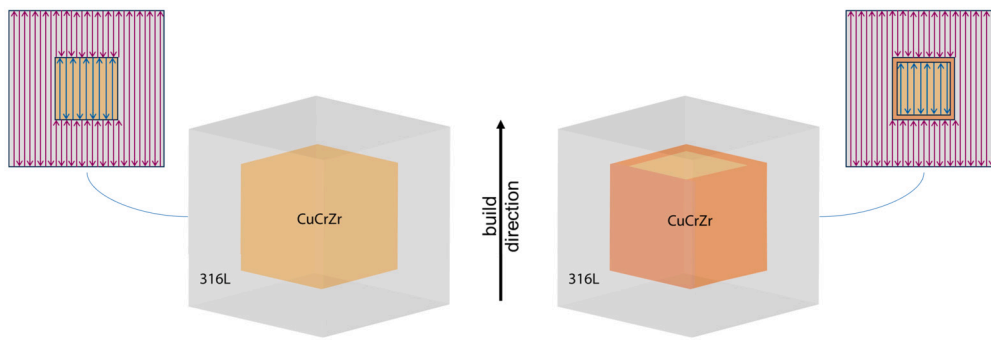


Fig. 2. Schematic of the samples geometry (not to scale): CuCrZr cubes embedded in 316L cubes. The darker lateral faces of the CuCrZr cube on the right drawing illustrate the faces where CuCrZr powder has not been melted in some samples, while the scan strategy within one layer is illustrated for each sample in the corresponding cross-sections (note that the remelting step of CuCrZr, performed with scan vectors rotated by 90° compared to the first melting, is not shown).

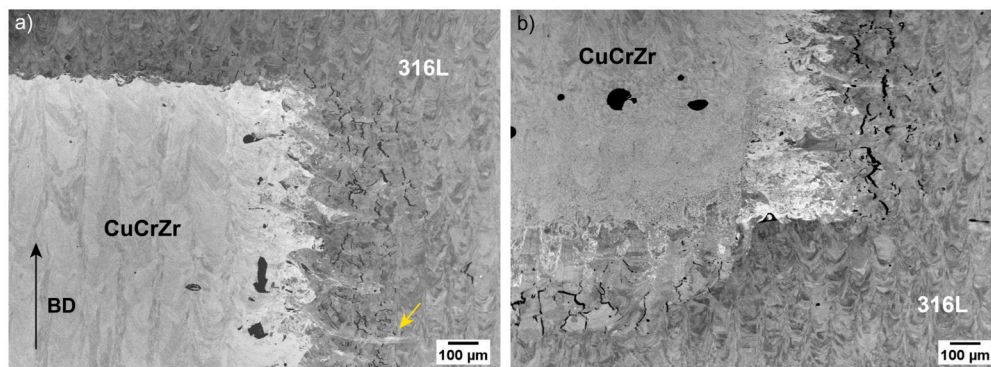


Fig. 3. Overview SEM/BSE images of an as-printed CuCrZr-316L sample: a) 316L on CuCrZr interface and b) CuCrZr on 316L interface. The vertical interface is visible on both images and the black arrow indicates the build direction (BD), which is oriented upwards with respect to the page.

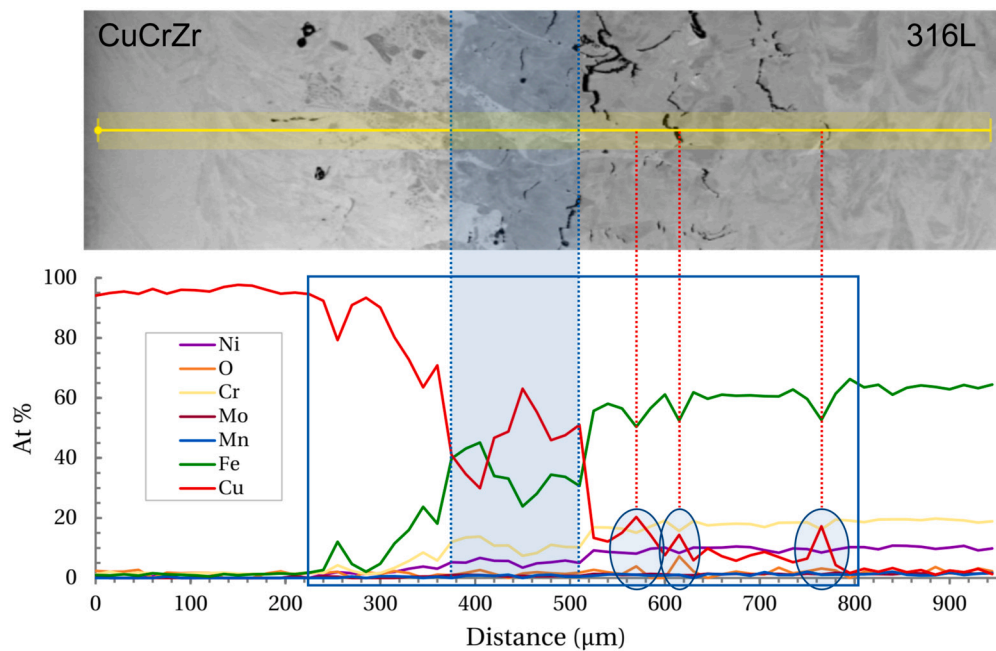


Fig. 4. EDX line profile across the vertical interface in the as-printed condition (total length of 945 μm, spacing of 15 μm between points, average of 4 lines separated by 10 μm). The red dashed lines show that peaks in Cu content are observed near the cracks present in 316L. The interface area is indicated by the light blue shaded area, whereas the total intermixing area is indicated by the solid blue frame.

left of this specific peak, extends beneath the surface at this location. Finally, despite the scatter in the data and the winding, diffuse character of the interface, it is possible to delineate an interface area within which the Cu and Fe contents are roughly equal, as indicated by the light blue

shaded area on the composition profile. One can then see that the diffusion length - estimated as the distance from the interface to the first data point with a content <2 at.% - of Cu in steel is about three times greater than that of Fe in Cu, with approximately 285 μm vs 95 μm.

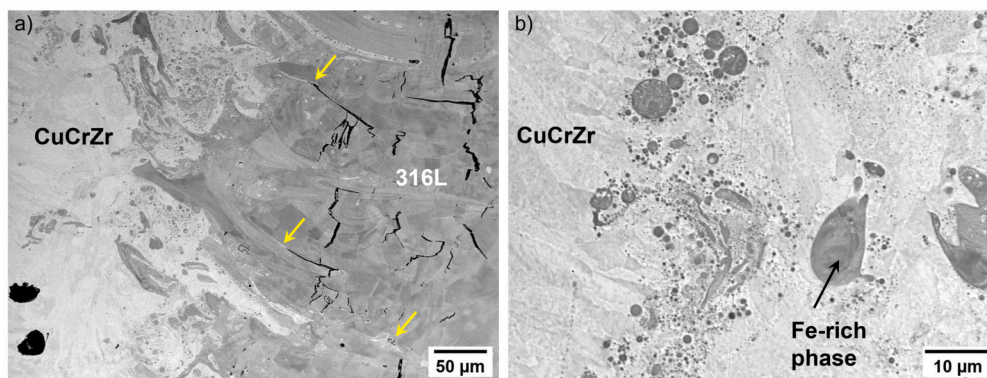


Fig. 5. As-printed sample: a) close-up view of the vertical interface between CuCrZr and 316L; b) demixing of the liquid into a Cu-rich liquid and an Fe-rich liquid near the interface (SEM/BSE).

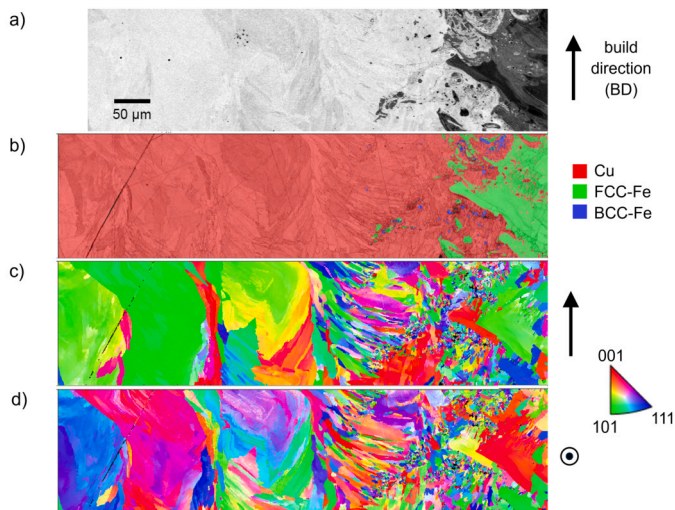


Fig. 6. a) BSE image, b) EBSD-EDX phase map, c) and d) EBSD orientation maps of the vertical CuCrZr-316L interface in the as-build condition. In c) and d), the color corresponds to the orientation with respect to the build direction and the indentation direction, respectively, with colors as indicated in the standard stereographic triangle.

At higher magnification, still in the as-built condition, the micrograph presented in the left image of Fig. 5 shows that cracks are often filled or at least partially filled with Cu, such as where indicated by the arrows. In the right image of Fig. 5, Fe droplets can be seen in Cu and Cu droplets in the steel. This demixing occurs due to the presence of a metastable liquid miscibility gap in the Cu-Fe system such that at high cooling rate, when the liquid is undercooled below a characteristic temperature, it enters the spinodal decomposition region and separates into an Fe-rich liquid and a Cu-rich liquid [38].

The EBSD maps presented in Fig. 6 show that very small, randomly-oriented Cu grains are present close to the interface with 316L, whereas further away large columnar grains growing parallel to the build direction can be distinguished. These columnar grains have  $\langle 101 \rangle$  axes preferentially oriented close to the build direction (image c), and either  $\langle 100 \rangle$  or  $\langle 111 \rangle$  orientation along the loading axis of the nanoindentation measurements presented later (image d). A small amount (1.86 vol.%) of BCC-Fe was also detected at the interface (image b).

### 3.2. Microstructure after HIP

Overview SEM images of a sample that was subjected to a HIP treatment after PBF-LB are given in Fig. 7. These micrographs show clearly that the pores and cracks that were present in the as-built state were successfully eliminated by the subsequent HIP treatment, both at the

horizontal and vertical interfaces between CuCrZr and 316L. Note that the visible black dots are not pores, but come from surface contamination that appears dark when using BSE contrast for imaging.

At the microscale, numerous Cu-rich channels can be observed in the steel, close to the vertical interface between the two materials and often at grain or sub-grain boundaries, as evidenced in Fig. 8, where a few of these white channels are indicated by arrows. These channels are found within the diffusion length of Cu into 316L, at locations that probably correspond to the locations of earlier cracks formed during PBF-LB.

The EBSD results presented in Fig. 9 show that the grain structure after HIP is very similar to that observed in the as-build state, i.e., the CuCrZr grains close to the interface are still very small, and the larger columnar CuCrZr grains have  $\langle 101 \rangle$  axes oriented close to the build direction (image c) and  $\langle 001 \rangle$  axes near the indentation loading direction (image d). One can also clearly see on the orientation maps that the large, approximately 100  $\mu\text{m}$  wide,  $\langle 101 \rangle$ -oriented grains are separated by thinner, elongated  $\langle 100 \rangle$ -oriented grains. The amount of BCC-Fe found near the interface (3.33 vol.%) is somewhat higher than in the as-built sample.

Overviews of the sample in which some CuCrZr powder was left unmelted close to the vertical interfaces with 316L, over a width of 100  $\mu\text{m}$ , are given in Fig. 10. As for the previous sample, this sample is also free of visible cracks and pores. However, it can be noticed that the sintered CuCrZr is not exactly located at the interface. Indeed, strong intermixing is still visible at the interface, evidencing that this region has been melted. On the other hand, small, rather equiaxed CuCrZr grains, which contrast with the large solidified columnar grains, are visible starting from a distance of approximately 100  $\mu\text{m}$  from the interface (Fig. 11, left). This offset is a consequence of the laser not being perfectly aligned with the deposited interfaces, and of the recoater being a mechanical system with limited deposition precision due to backlash and the different thermal expansion of its components.

Cu channels can again be distinguished in the steel, close to the interface, whereas some precipitates and inclusions are visible in the CuCrZr (Fig. 11, right). Elemental mappings acquired by EDX and given in Fig. 12 reveal that the smaller precipitates which decorate the grain boundaries are mostly Fe- and Cr-rich particles. The larger inclusions are found to be mixed (Cr,Fe) oxide particles, and a few Zr-rich particles are also found at grain boundaries and in contact with the oxide inclusions. Note that these inclusions, which were not observed in the as-built condition, are found both in the sintered and in the previously solidified CuCrZr grains.

The EDX line profile presented in Fig. 13 shows that after HIP the intermixing spans over a thickness of roughly 670  $\mu\text{m}$ , while the diffusion length of Fe into CuCrZr and that of Cu into 316L are respectively of 75 and 405  $\mu\text{m}$ . Therefore, only the diffusion of Cu into 316L is more pronounced after HIP, compared to the as-built condition (285  $\mu\text{m}$ ). The diffusion length of Fe in Cu is found to be of the same order of magni-

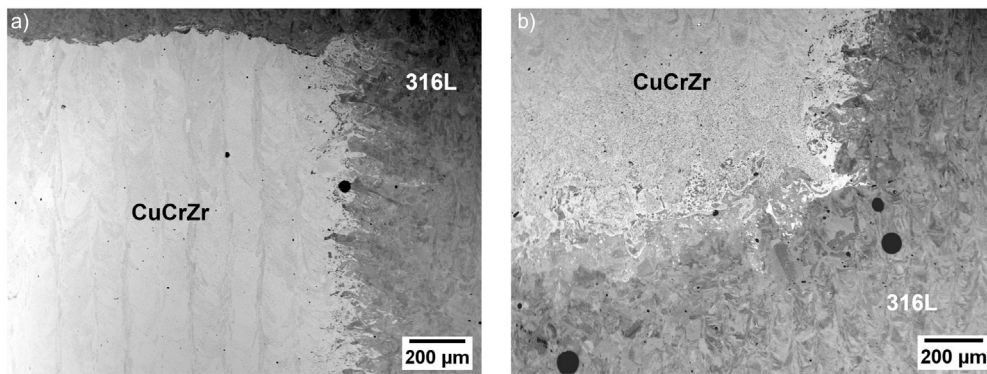


Fig. 7. Overview SEM/BSE images of a CuCrZr-316L sample where major printing defects were suppressed by a post-build HIP treatment: a) 316L on CuCrZr interface and b) CuCrZr on 316L interface.

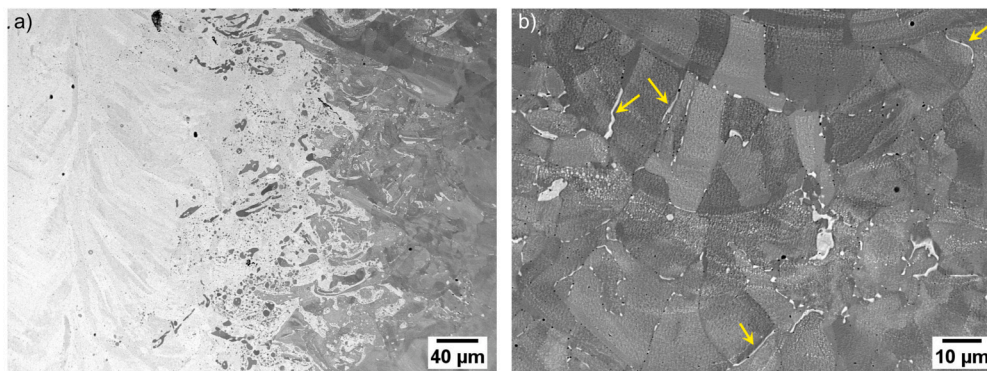


Fig. 8. CuCrZr-316L sample after the post-build HIP treatment: close views of a) the vertical interfacial area and b) Cu channels present in 316L, close to the interface (SEM/BSE).

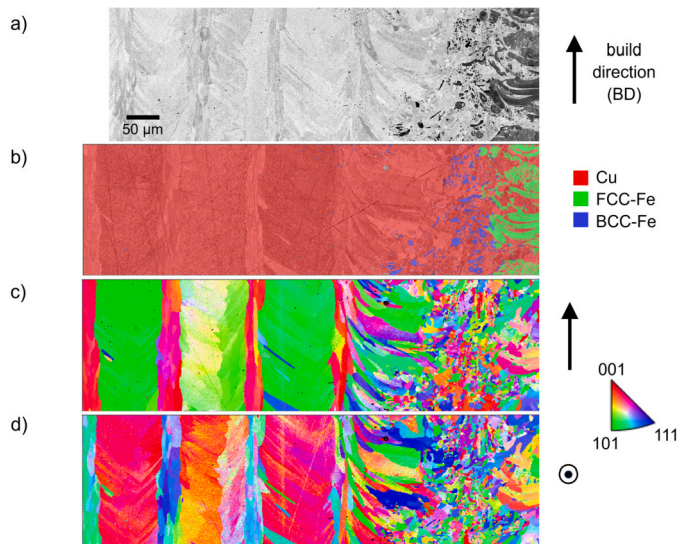


Fig. 9. a) BSE image, b) EBSD-EDX phase map, c) and d) EBSD orientation maps of the CuCrZr-316L interface after HIP. In c) and d), the color corresponds to the orientation with respect to the build direction and the indentation direction, respectively, with colors as indicated in the standard stereographic triangle.

tude than in the as-built condition (95  $\mu\text{m}$ ), the difference being within the variation induced by the waviness of the interface, which is however difficult to precisely quantify. Note also that some peaks of oxygen are detected in the CuCrZr, due to the presence of the oxide inclusions described above.

In this sample where some CuCrZr powder was sintered, EBSD orientation maps (Fig. 14 c and d) show that very small Cu grains are

still observed close to the interface, whereas small, randomly-oriented sintered grains are found a bit further from the interface, followed by larger columnar grains further away. The few large columnar grains that were analyzed in this area have either  $\langle 111 \rangle$  or  $\langle 100 \rangle$  orientation parallel to the build direction and the indentation loading axis. The phase map in Fig. 14 b) shows a similar amount of BCC-Fe (2.95 vol.%) than in the previous sample.

### 3.3. Nanoindentation

Hardness  $H$  and reduced modulus  $E_r$  maps acquired across the horizontal interfaces where CuCrZr was melted on top of 316L are given in Figs. 15 and 16. For all three samples, a gradual increase in hardness and modulus can be observed from CuCrZr towards 316L. Note that data were acquired over a smaller area in the as-built sample (450  $\times$  150  $\mu\text{m}$  versus 800  $\times$  150  $\mu\text{m}$  for the HIPed samples), because of the presence of numerous cracks and pores which make nanoindentation difficult.

Nevertheless, it can be seen in Fig. 15 that the HIP treatment results in a general softening of the CuCrZr, with the bulk hardness of CuCrZr,  $H_{\text{CuCrZr}}$ , being in the range 2.5-3 GPa in the as-built sample and 1.5-2 GPa after HIP. Within the highly intermixed regions, hardness is locally higher in Fe-rich areas. Especially the small Fe-rich droplets that are visible within the CuCrZr show high hardness values ( $\sim$  9-10 GPa).

The reduced modulus maps presented in Fig. 16 do not show significant differences before and after HIP, over the areas that were measured. The modulus on the CuCrZr side appears to be slightly lower in the sample HIPed with no powder left unmelted ( $\sim$  135 GPa), compared to the other HIPed sample ( $\sim$  145 GPa), which shows values close to the as-built sample, although the same processing parameters were used for printing these interfaces in both samples subjected to HIP (powder was left unmelted at vertical interfaces only).

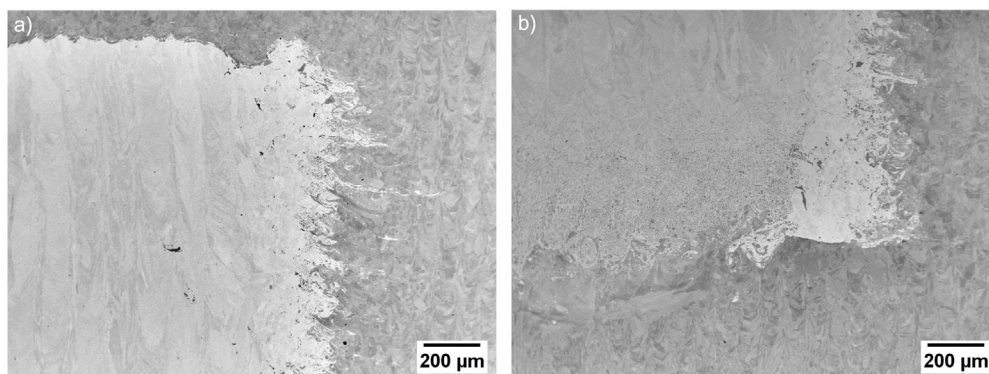


**Fig. 10.** Overview SEM/BSE images of a CuCrZr-316L sample where CuCrZr powder close to the vertical interface with 316L was not melted during PBF-LB and which was subjected to a post-build HIP treatment: a) 316L on CuCrZr interface and b) CuCrZr on 316L interface.

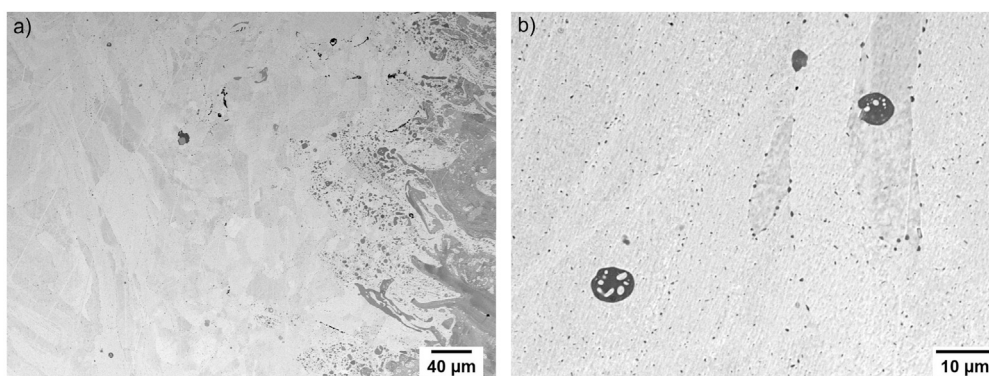


**Fig. 11.** a) A roughly 100-150  $\mu\text{m}$ -thick layer with small equiaxed grains can be seen on the CuCrZr side of the interface; b) higher magnification image showing the presence of different inclusions in the CuCrZr (SEM/BSE).

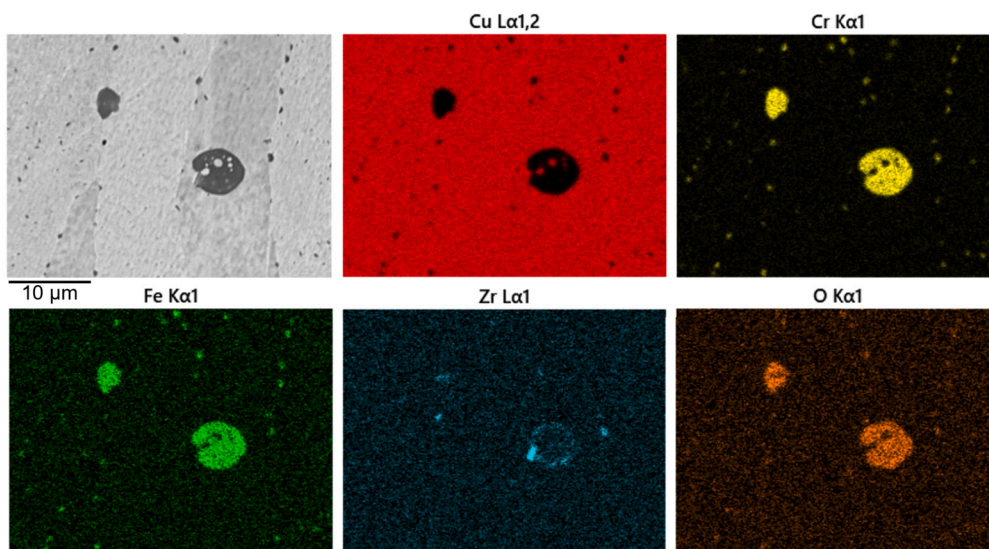


**Fig. 12.** Elemental mappings of CuCrZr area with different inclusions and precipitates.

Hardness and reduced modulus maps acquired across vertical interfaces are shown in Figs. 17 and 18. Note that the sharp vertical lines visible in a) as a dark blue line close to the interface and in c) as a dark red line in the steel are measurement artifacts. As in the case of horizontal interfaces, both hardness and reduced modulus are found to increase progressively from CuCrZr to 316L. It is also interesting to note that in the as-built sample, the hardness of CuCrZr near the vertical interface with 316L (in the range 2.5-2.9 GPa) appears to be lower than the values found close to the horizontal interface with 316L (in the

range 3-3.4 GPa). HIP again results in a global softening of the CuCrZr, but to a much lesser relative extent in this case. After HIP, the hardness of CuCrZr in the vicinity of 316L is slightly higher in the vertical compared to the horizontal configurations.

The reduced modulus maps of vertical interfaces show overall higher values compared to horizontal interfaces. For the bulk CuCrZr,  $E_r$  is in the range 160-170 GPa for all three samples. In Fig. 18 b), one can also observe on the CuCrZr side higher modulus values in the thinner columnar grains. This effect can also be seen in the as-built sample.



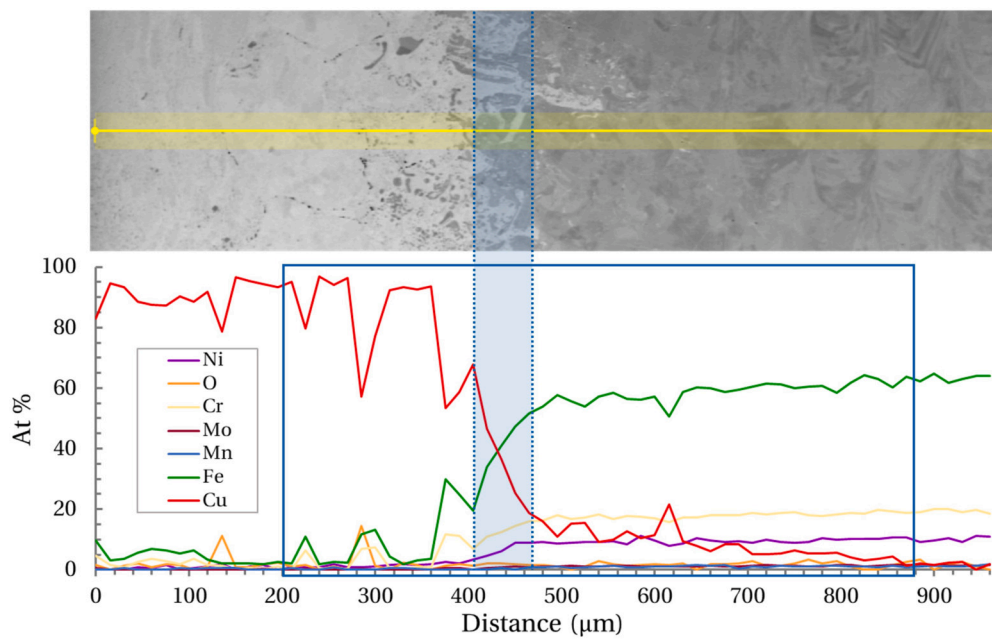


Fig. 13. EDX composition profile (in atomic %) across the vertical interface after the HIP treatment (total length of 960  $\mu\text{m}$ , spacing of 15  $\mu\text{m}$  between points, average of 4 lines separated by 10  $\mu\text{m}$ ).

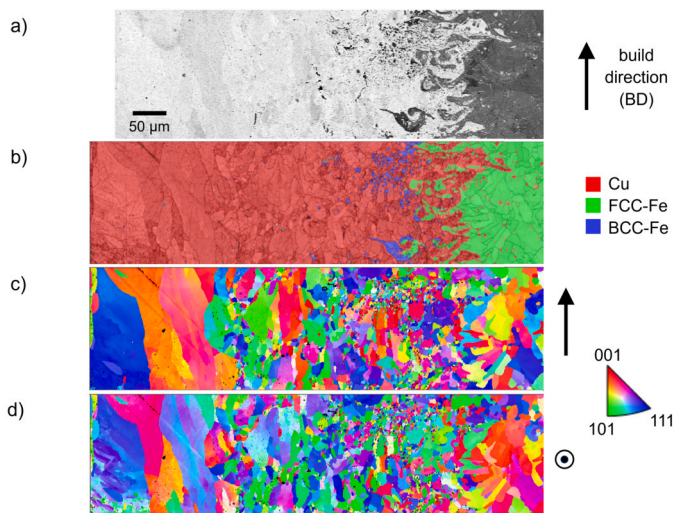


Fig. 14. a) BSE image, b) EBSD-EDX phase map, c) and d) EBSD orientation maps of the CuCrZr-316L interface after HIP with some sintered CuCrZr. In c) and d), the color corresponds to the orientation with respect to the build direction and the indentation direction, respectively, with colors as indicated in the standard stereographic triangle.

## 4. Discussion

### 4.1. As-built defects and their elimination

The MM-PBF-LB process is observed to lead to the formation of significant defects at the interface between CuCrZr and 316L, as in most MM-PBF-LB studies of Cu alloys and steels reported in the literature.

Large irregularly-shaped pores are observed in PBF-LB-printed CuCrZr, especially close to the interfaces with 316L. In PBF-LB, the most common sources of porosity are: lack of fusion, gas entrapment, key-holing, ejection of metal particles and balling (instability of the melt due to a poor wettability). Keyhole pores result from material evaporation and are typically spherical, relatively small and located at the bottom of the melt pools, i.e., do not correspond to the pores observed

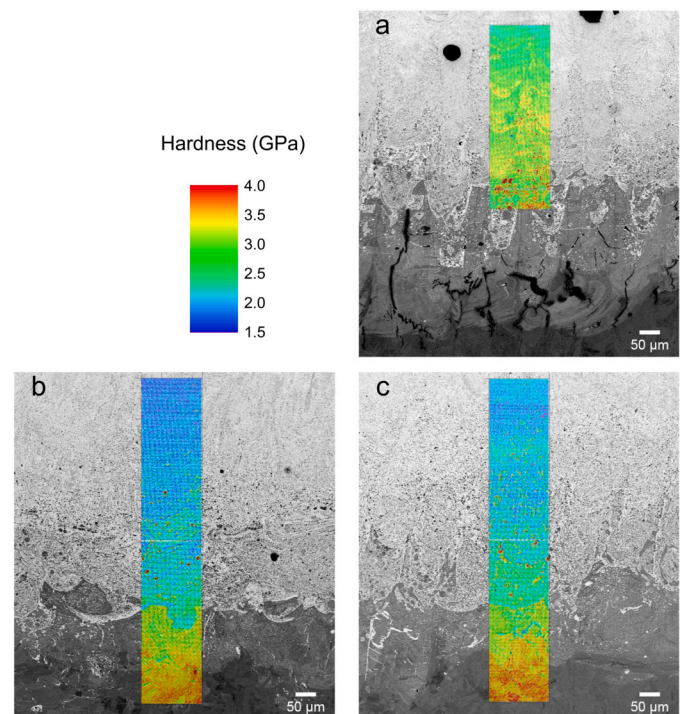
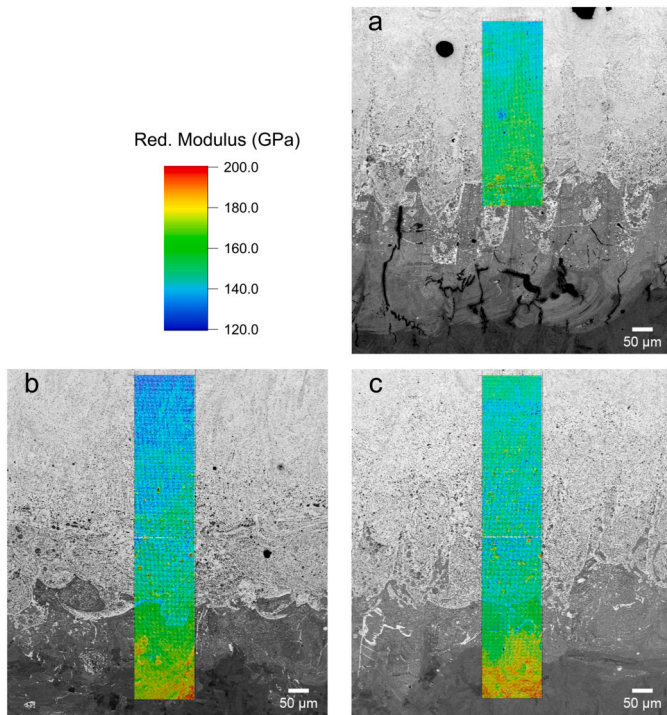
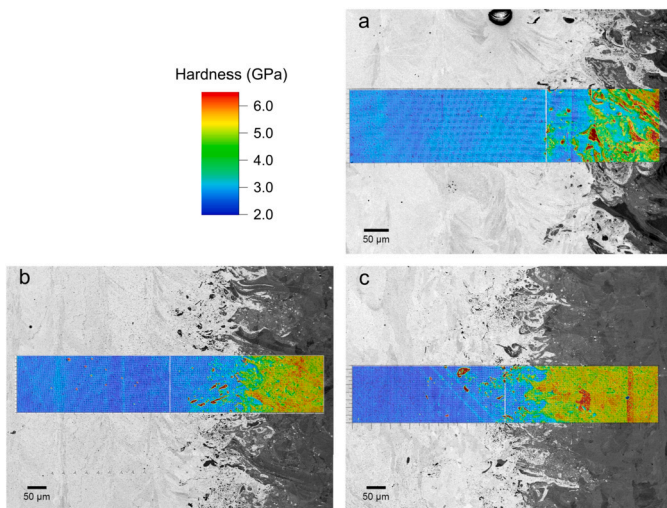


Fig. 15. Nanoindentation hardness maps across horizontal CuCrZr-316L interfaces: a) as-built, b) after HIP with all the powder melted and c) after HIP with 100  $\mu\text{m}$  of CuCrZr powder not melted at the vertical interfaces with 316L.

here. Pores resulting from gas entrapment, including dissolved hydrogen from water adsorption at the particles surface, are also typically spherical. Therefore, despite the sensitivity of CuCrZr to humidity, gas entrapment can be ruled out, too. Lack-of-fusion (LoF) pores can be formed when the energy input is too low and the melt solidifies without enough remelting of the previous layer, or when adjacent tracks do not sufficiently overlap. Unlike pores resulting from keyholing or gas entrapment, LoF pores have an irregular shape, such that insufficient melting is a possible cause for the pores observed in the present sam-



**Fig. 16.** Reduced modulus maps across horizontal CuCrZr-316L interfaces: a) as-built, b) after HIP with all the powder melted and c) after HIP with 100 μm of Cu powder not melted.



**Fig. 17.** Hardness maps across vertical CuCrZr-316L interfaces: a) as-built, b) after HIP with all the powder melted and c) after HIP with 100 μm of Cu powder not melted.

ples. In fact, LoF porosity was observed by Liu et al. in C18400 alloy when printed on top of 316L [31]. Although no explanation is provided by Bai et al. [36] for the pores present in C52400 alloy printed on top of 316L, those also look similar to LoF pores. Concerning the pores observed in CuSn10 by Wei et al., these are specific to the deposition setup used, which creates an uneven surface of the second material [24,25]. However, looking at the location of the current pores in CuCrZr with respect to the edge of the sample, one can see that this compares well with the length of the scan vector on the 316L side (3 mm), as shown in the optical micrograph presented in Fig. 19. Therefore, the porosity observed at proximity of the vertical interface is likely resulting from the powder bed misalignment with respect to the laser. As a consequence, the copper close to the interface was scanned with the laser param-

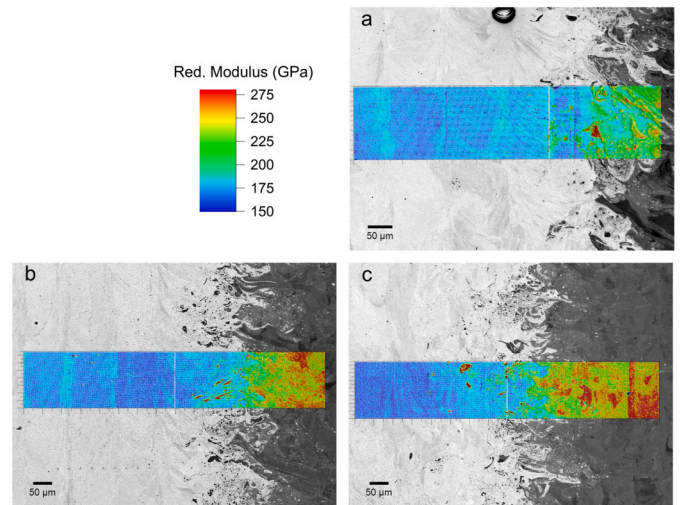


**Fig. 18.** Reduced modulus maps across vertical CuCrZr-316L interfaces: a) as-built, b) after HIP with all the powder melted and c) after HIP with 100 μm of Cu powder not melted.

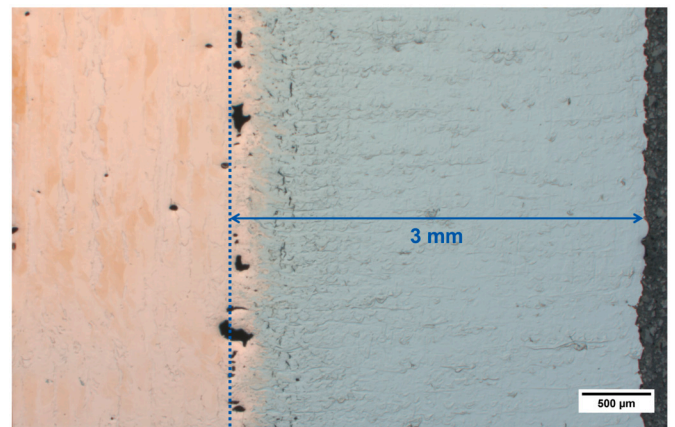


**Fig. 19.** Optical micrograph of as-built sample showing that the large pores present within the CuCrZr are located at a distance of approximately 3 mm from the edge of the sample, i.e., close to end of the scan vectors used to melt the 316L powder.

ters of the steel, i.e., with an energy density that was not sufficient to properly melt the copper. This is also supported by the fact that the vertical interface between CuCrZr and 316L was still melted in the sample designed to have CuCrZr powder left unmelted.

Another possibility is that the porosity observed close to the interfaces arises from the unavoidable cross-contamination occurring during the recoating of a multi-material powder bed, and which would also explain why the pores are observed only close to the interfaces. Indeed, where 316L particles are present within the CuCrZr powder bed, this is likely to result in the formation of solid spatters as described in [39]: 316L is vaporized due to a too high energy input, and outside of the strong laser interaction region, unmelted CuCrZr powder particles are ejected by the vapor jet thus created before they could be melted by the laser beam. Such a mechanism could thus also explain some of the pores present in the as-fabricated state, especially the smaller ones located close to the horizontal interface where CuCrZr was printed on top of 316L.

The cracks observed in the steel close to the interfaces with Cu are likely to be due to the copper contamination cracking phenomenon. 316L steel is known to be embrittled by the penetration of liquid Cu at grain boundaries, which leads to cracking when high tensile stresses are present within the steel, as described in the Introduction section. Tensile

stresses arise in single-material AM parts because the solidification and thermal shrinkage of the molten pool is constrained by the surrounding material. In MM-PBF-LB of Cu and steel, residual stresses might even be higher since they also arise from thermal conductivity and CTE mismatches between the two materials. The printing sequence used for vertical interfaces, i.e., melting of steel followed by melting (and remelting) of CuCrZr, is not optimal to limit thermal stresses and cracking in the steel near the interface. However, when CuCrZr is scanned first, due to the high energy input needed to melt the CuCrZr, steel powder particles close to the interface tend to be ejected from the powder bed, resulting in a large amount of porosity. This contradiction in the optimal scanning sequence represents a major motivation for sintering, rather than melting the powder near the interface.

The Cu present at the surface of the cracks after PBF-LB is found as Cu-rich (sub-) grain boundaries channels in the steel after HIP. During HIP, where no tensile stresses act on the steel, the presence of copper at the steel grain boundaries can be beneficial and help to close the cracks, thanks to a higher atomic mobility (lower melting point).

#### 4.2. Intermixing

The as-built condition showed that there is more mixing when Cu is deposited on steel than when steel is deposited on Cu, similarly to literature observations for different steel grades and Cu alloys [23,27,36], and which is mostly due to the higher laser power needed to melt the CuCrZr powder.

Intermixing at vertical interfaces extends over long distances (600–700  $\mu\text{m}$ ), driven by large Marangoni convection. Surface tension gradients within the melt pool are due to both temperature differences and compositional variations. Thermodynamic simulations showed that for a 50 wt.% CuCrZr - 50 wt.% 316L composition, assuming Scheil solidification, the Fe-rich and Cu-rich liquids coexist in the temperature range  $\sim 1350\text{--}1375^\circ\text{C}$  [30]. At a temperature of  $1350^\circ\text{C}$ , 316L has a surface tension of 1.47 N/m (based on data from [40], for a 316L steel with similar S content), while the surface tension of pure Cu (no data could be found for CuCrZr) is 1.36 N/m [41], i.e., is 7% lower than that of 316L. Intermixing is further accentuated by the fact that the laser was not perfectly aligned with the deposited powder pattern - because this alignment can be performed with an accuracy of the order of 100  $\mu\text{m}$  only - which resulted in melting of the interface even when some Cu powder was left unmelted, and dragging of liquid Cu into the steel when the laser scans the interface with a direction perpendicular to it.

In addition to the strong intermixing taking place in the liquid state, solid-state interdiffusion occurs during the repeated thermal cycles associated with the addition of subsequent layers and during the post-PBF-LB HIP treatment. Since the interdiffusion coefficient  $\bar{D}$  can be expressed as  $X_{Fe}D_{Cu} + X_{Cu}D_{Fe}$  (Darken's equation, with  $X_i$  and  $D_i$  the molar fraction and self-diffusion coefficient of species  $i$ , respectively), in the Cu-rich area of the interface, the interdiffusion coefficient should be close to  $D_{Fe}$  and thus less pronounced than the diffusion of Cu into the steel, since at a given temperature  $D_{Fe} < D_{Cu}$ , which is in agreement with the experimental observations. Also, the penetration of liquid Cu into the grain boundaries of the steel further accelerates the diffusion of Cu in steel during the PBF-LB process. Moreover, the temperature of the HIP process corresponds to  $0.98 \times T_{m,Cu}$  and  $0.73 \times T_{m,Fe}$  and after HIP, only the diffusion length of Cu into the steel is significantly longer than in the as-built condition.

#### 4.3. CuCrZr texture

To the best of our knowledge, the texture observed in the bulk CuCrZr of the present samples, i.e., large columnar grains with a  $\langle 101 \rangle$  preferential orientation parallel to the build direction, separated by thinner grains with  $\langle 001 \rangle$  orientation parallel to the build direction, has not been reported yet. However, the texture of PBF-LB-printed CuCrZr has been shown to depend on the laser parameters used. Jadhav

et al. [42] observed that the top surface shows a texture that depends on the applied scan parameters: a low scan speed (200 mm/s) favors a strong  $\langle 100 \rangle$  texture parallel to the build direction, whereas at higher speed (400 mm/s) a weak  $\langle 110 \rangle$  texture develops. In contrast, these authors found that this texture was erased in the bulk CuCrZr, which showed a relatively random crystal orientation. The texture observed in the present study probably arises from the specific scanning strategy used, with  $90^\circ$  interlayer rotation and a remelting step that was also performed with a rotation of  $90^\circ$  compared to the first melting.

#### 4.4. Micro-mechanical properties

Concerning mechanical properties, the bulk CuCrZr is harder in the as-built condition than after HIP. Due to the fast cooling rate inherent to the PBF-LB process, solute elements (especially Cr) are prevented from precipitating in the solid state and contribute to significant solution strengthening. Compressive residual stresses are also likely to contribute to hardening, as the tensile stresses that develop in PBF-LB during solidification are typically transformed into compressive stresses upon addition of the following layers, so that most of the volume of the cubic samples is ultimately under compressive stresses. After HIP, the hardness of the bulk CuCrZr is lower partly due to the precipitation of Cr (and Zr) during the high-temperature holding, since at equilibrium the solubility of Cr (and Zr) in Cu is almost non-existent, and partly to the relief of residual stresses.

Close to the interfaces with 316L, CuCrZr shows very fine grains after solidification, which makes it harder than the bulk CuCrZr. The formation of these very small grains is consistent with the EBSD observations of [31] and [32] on different Cu alloys built on top of steel, and can be due to different mechanisms, such as already solidified Fe droplets acting as nucleation sites, given the similarity in lattice parameters between FCC Cu and Fe, or partitionless solidification. Partitionless solidification can occur if the undercooling is so high that nucleation occurs at a temperature below the extended solidus line, which is more likely to happen with a high Fe content, resulting in the formation of a fine equiaxed structure as multiple nucleation events occur [43]. In addition to grain boundary strengthening, solute strengthening by Fe atoms is not expected to contribute significantly to hardening, as Fe and Cu have similar atomic radii (132 pm), but the presence of dispersed, fine Fe precipitates is likely to play a role. The small grains are still visible after HIP, meaning that significant grain growth is effectively prevented by the fine Fe- and Cr-rich precipitates present at grain boundaries. Harder areas are still visible after HIP, but to a lesser extent, probably due to a combined effect of stress relief and Cr precipitation.

In the as-built sample, CuCrZr hardness values measured close to the vertical interface with 316L are overall lower than those measured near the horizontal interface. This might come from differences in density, since numerous pores are visible in the CuCrZr at proximity of the vertical interface. This assumption is supported by the values measured after HIP, in the sample where all the powder was melted: in that case the hardness of CuCrZr close to the horizontal interface (2–2.4 GPa) is observed to be lower than close to the vertical interface (2.4–2.7 GPa) and is mostly determined by the amount of Fe dissolved into the Cu.

Whereas columnar as-solidified grains are observed both in the 316L and CuCrZr, CuCrZr sintered grains appear more globular. However, overall hardness and modulus values do not vary much between sintered and columnar Cu grains. This suggests that the micro-mechanical properties of CuCrZr after HIP are not affected by this difference in grain morphology. On the other hand, the large  $\langle 101 \rangle$ -oriented columnar CuCrZr grains show smaller values of modulus compared to the thinner  $\langle 100 \rangle$ -oriented grains. Pure Cu has been shown to exhibit significant anisotropy in elastic modulus, with a Young's modulus along  $\langle 001 \rangle$  direction that is about half that measured parallel to the  $\langle 110 \rangle$  direction, and  $0.3\times$  that of the  $\langle 111 \rangle$  direction [44]. According to the EBSD orientation maps with respect to the loading axis during nanoindentation, the larger grains are measured with a loading direction that is

close to their  $\langle 001 \rangle$  axis, whereas the thinner grains are measured in a direction closer to either  $\langle 110 \rangle$  or  $\langle 111 \rangle$  axes. Therefore, the trend measured in the present samples is in line with published data.

## 5. Conclusions

The following conclusions can be drawn from the present investigation:

- In terms of the integrity of the CuCrZr-316L parts produced, a post-PBF-LB HIP treatment is found to be effective in closing the numerous cracks and pores that are visible in the vicinity of CuCrZr-316L interfaces after multi-material PBF-LB processing of the two alloys.
- Mechanical properties are affected by the HIP treatment, especially those of CuCrZr. After PBF-LB, the hardness of CuCrZr close to the interfaces with 316L is higher than that of the bulk CuCrZr, thanks to a combined strengthening effect of the fine Fe particles formed by spinodal decomposition and a locally very fine grain size. After the HIP treatment, an overall decrease in hardness of the bulk CuCrZr is observed, due to the relief of residual stresses and the precipitation of Cr and Zr. However, CuCrZr remains harder close to the interface with steel, as the fine-grained structure is retained during HIP, which is believed to arise from the grain boundary pinning effect of very fine Cr- and Fe-rich precipitates. Beyond mechanical properties, it is important to mention that the precipitation of elements trapped in solid solution during the fast cooling of the PBF-LB process is however beneficial for applications that seek a high electrical or thermal conductivity.
- Compared to full melting of the interface, leaving a thickness of unmelted CuCrZr powder close to the interface with 316L seems to produce no noticeable differences in mechanical properties after HIP. This strategy could still be interesting to create sharper interfaces between the two materials. However, misalignment between the laser and the deposited powder pattern inevitably results in a high risk of melting the interface, even when some powder is not melted, leading to an extended zone of intermixing. To reduce this intermixing, and thus enable the fabrication of bi-metallic components with sharp interfaces, it is therefore recommended to leave some unmelted powder on both sides of the interface.

It has to be noted that one limitation of the combined MM-PBF-LB and HIP approach proposed here is that interfaces need to be internal, i.e., they need to be enclosed within an airtight outer shell, provided here by the 316L outer cube, in order for HIP to be effective, which limits the design freedom of multi-material components. However, this limitation can easily be overcome by adding a thin outer single-material shell. The build orientation of the part needs also to be carefully chosen, as for support reason, powder cannot be left unmelted at horizontal interfaces during the PBF-LB process. Nevertheless, the method proposed here has great potential for the production of defect-free bimetallic components made of copper and steel, as printing defects are eliminated by the HIP treatment regardless of orientation.

In an industrial context, the additional HIP treatment might increase production costs and time compared with PBF-LB alone. However, HIP is already common practice for applications that require very low residual porosity, such as in the aerospace industry. Furthermore, if a subsequent HIP process is performed, the printing process can be accelerated by using higher layer thicknesses and scanning speeds, thus reducing costs, as it is then not necessary to aim for 100% density after printing, as long as closed porosity is achieved and distortion remains limited during HIP.

## CRedit authorship contribution statement

**L. Deillon:** Writing – original draft, Visualization, Investigation, Funding acquisition, Conceptualization. **N. Abando Beldarrain:** Writing – review & editing, Investigation. **X. Li:** Writing – review & editing, Resources, Conceptualization. **M. Bambach:** Supervision, Funding acquisition, Conceptualization, Writing – review & editing.

ing – review & editing, Investigation. **X. Li:** Writing – review & editing, Resources, Conceptualization. **M. Bambach:** Supervision, Funding acquisition, Conceptualization, Writing – review & editing.

## Declaration of competing interest

The authors declare that they have no known competing financial interests or personal relationships that could have appeared to influence the work reported in this paper.

## Data availability

Data will be made available on request.

## Acknowledgements

The authors would like to thank Mr Felix Jensch at BTU Cottbus for performing the HIP treatment, Mrs Caroline Pereira Martendal for performing the EBSD measurements and the SFA Advanced Manufacturing program of the ETH Board for funding this research through the “Multi-Mat” project.

## References

- [1] C. Wei, L. Li, Recent progress and scientific challenges in multi-material additive manufacturing via laser-based powder bed fusion, *Virtual Phys. Prototyping* 16 (3) (2021) 1–25, <https://doi.org/10.1080/17452759.2021.1928520>, <https://www.tandfonline.com/doi/full/10.1080/17452759.2021.1928520>.
- [2] M. Schneck, M. Horn, M. Schmitt, C. Seidel, G. Schlick, G. Reinhart, Review on additive hybrid- and multi-material-manufacturing of metals by powder bed fusion: state of technology and development potential, *Prog. Addit. Manuf.* 6 (2021) 881–894, <https://doi.org/10.1007/s40964-021-00205-2>.
- [3] D. Wang, L. Liu, G. Deng, C. Deng, Y. Bai, Y. Yang, W. Wu, J. Chen, Y. Liu, Y. Wang, X. Lin, C. Han, Recent progress on additive manufacturing of multi-material structures with laser powder bed fusion, *Virtual Phys. Prototyping* 17 (2) (2022) 329–365, <https://doi.org/10.1080/17452759.2022.2028343>.
- [4] J. Guan, Q. Wang, Laser powder bed fusion of dissimilar metal materials: a review, *Materials* 16 (7) (2023) 2757, <https://doi.org/10.3390/ma16072757>, <https://www.mdpi.com/1996-1944/16/7/2757>.
- [5] B. Neirincx, X. Li, M. Hick, Powder deposition systems used in powder bed-based multimetal additive manufacturing, *Acc. Mater. Res.* 2 (6) (2021) 387–393, <https://doi.org/10.1021/accountsmr.1c00030>.
- [6] S.L. Sing, S. Huang, G.D. Goh, G.L. Goh, C.F. Tey, J.H. Tan, W.Y. Yeong, Emerging metallic systems for additive manufacturing: in-situ alloying and multi-metal processing in laser powder bed fusion, *Prog. Mater. Sci.* 119 (jun 2021), <https://doi.org/10.1016/j.pmatsci.2021.100795>.
- [7] A. Mannucci, I. Tomashchuk, V. Vignal, P. Sallamand, M. Duband, Parametric study of laser welding of copper to austenitic stainless steel, *Proc. CIRP* 74 (2018) 450–455, <https://doi.org/10.1016/j.procir.2018.08.160>.
- [8] G. Wilde, R. Willnecker, R.N. Singh, F. Sommer, The metastable miscibility gap in the system Fe-Cu, *Z. Met. (Mater. Res. Adv. Tech.)* 88 (10) (1997) 804–809.
- [9] W.F. Savage, E.F. Nippes, M.C. Mushala, Liquid-metal embrittlement of the heat-affected zone by copper contamination, *Weld. J.* 57 (5) (1978) 2375–2455.
- [10] S. Rao, A.Y. Al-Kawaie, Copper contamination cracking in austenitic stainless steel welds, *Weld. J.* 89 (2) (2010) 46–49.
- [11] B. Joseph, M. Picat, F. Barbier, Liquid metal embrittlement: a state-of-the-art appraisal, *Eur. Phys. J. Appl. Phys.* 5 (1999) 19–31.
- [12] J.E. Norkett, M.D. Dickey, V.M. Miller, A review of liquid metal embrittlement: cracking open the disparate mechanisms, *Metall. Mater. Trans. A, Phys. Metall. Mater. Sci.* 52 (6) (2021) 2158–2172, <https://doi.org/10.1007/S11661-021-06256-Y/FIGURES/11>, <https://link.springer.com/article/10.1007/s11661-021-06256-y>.
- [13] C. Lampa, J. Powell, C. Magnusson, Laser welding of copper to stainless steel, *Laser Inst. Am., Proc.* 83 (2) (1997), <https://doi.org/10.2351/1.5059720>.
- [14] S. Chen, J. Huang, J. Xia, H. Zhang, X. Zhao, Microstructural characteristics of a stainless steel/copper dissimilar joint made by laser welding, *Metall. Mater. Trans. A* 44 (8) (2013) 3690–3696, <https://doi.org/10.1007/s11661-013-1693-z>, <http://link.springer.com/10.1007/s11661-013-1693-z>.
- [15] S. Chen, J. Huang, J. Xia, X. Zhao, S. Lin, Influence of processing parameters on the characteristics of stainless steel/copper laser welding, *J. Mater. Process. Technol.* 222 (2015) 43–51, <https://doi.org/10.1016/j.jmatprotec.2015.03.003>.
- [16] T. Suga, Y. Murai, T. Kobashi, K. Ueno, M. Shindo, K. Kanno, K. Nakata, Laser brazing of a dissimilar joint of austenitic stainless steel and pure copper, *Weld. Int.* 30 (3) (2016) 166–174, <https://doi.org/10.1080/09507116.2014.921090>.
- [17] G.R. Joshi, V.J. Badheka, Processing of bimetallic steel-copper joint by laser beam welding, *Mater. Manuf. Process.* 34 (11) (2019) 1232–1242, <https://doi.org/10.1080/10426914.2019.1628262>.

- [18] J. Li, Y. Cai, F. Yan, C. Wang, Z. Zhu, C. Hu, Porosity and liquation cracking of dissimilar Nd: YAG laser welding of SUS304 stainless steel to T2 copper, *Opt. Laser Technol.* 122 (2020) 105881, <https://doi.org/10.1016/j.optlastec.2019.105881>, July 2019.
- [19] S. Chen, X. Yu, J. Huang, J. Yang, S. Lin, Interfacial ferrite band formation to suppress intergranular liquid copper penetration of solid steel, *J. Alloys Compd.* 773 (2019) 719–729, <https://doi.org/10.1016/j.jallcom.2018.09.282>.
- [20] T.A. Mai, A.C. Spowage, Characterisation of dissimilar joints in laser welding of steel-kovar, copper-steel and copper-aluminium, *Mater. Sci. Eng. A* 374 (1–2) (2004) 224–233, <https://doi.org/10.1016/j.msea.2004.02.025>.
- [21] S.V. Kuryntsev, A.E. Morushkin, A.K. Gilmudinov, Fiber laser welding of austenitic steel and commercially pure copper butt joint, *Opt. Lasers Eng.* 90 (2017) 101–109, <https://doi.org/10.1016/j.optlaseng.2016.10.008>, October 2016.
- [22] J. Chen, Y. Yang, C. Song, M. Zhang, S. Wu, D. Wang, Interfacial microstructure and mechanical properties of 316L /CuSn10 multi-material bimetallic structure fabricated by selective laser melting, *Mater. Sci. Eng. A* 752 (February 2019) 75–85, <https://doi.org/10.1016/j.msea.2019.02.097>.
- [23] C. Anstaett, C. Seidel, G. Reinhart, Fabrication of 3D multi-material parts using laser-based powder bed fusion, in: *Solid Freeform Fabrication 2017: Proceedings of the 28th Annual International Solid Freeform Fabrication Symposium, 2017*, pp. 1548–1556, <http://utw10945.utweb.utexas.edu/sites/default/files/2017/Manuscripts/Fabricationof3DMultiMaterialPartsUsingLaser.pdf>.
- [24] C. Wei, L. Li, X. Zhang, Y.-h. Chueh, 3D printing of multiple metallic materials via modified selective laser melting, *CIRP Ann.* 67 (1) (2018) 245–248, <https://doi.org/10.1016/j.cirp.2018.04.096>.
- [25] C. Wei, Z. Sun, Y. Huang, L. Li, Embedding anti-counterfeiting features in metallic components via multiple material additive manufacturing, *Addit. Manuf.* 24 (September 2018) 1–12, <https://doi.org/10.1016/j.addma.2018.09.003>.
- [26] C. Wei, Z. Sun, Q. Chen, Z. Liu, L. Li, Additive manufacturing of horizontal and 3D functionally graded 316L/Cu10Sn components via multiple material selective laser melting, *J. Manuf. Sci. Eng., Trans. ASME* 141 (8) (2019) 1–8, <https://doi.org/10.1115/1.4043983>.
- [27] O. Al-Jamal, S. Hinduja, L. Li, Characteristics of the bond in Cu–H13 tool steel parts fabricated using SLM, *CIRP Ann.* 57 (1) (2008) 239–242, <https://doi.org/10.1016/j.cirp.2008.03.010>.
- [28] M. Oel, J. Rossmann, B. Bode, I. Meyer, T. Ehlers, C.M. Hackl, R. Lachmayer, Multi-material laser powder bed fusion additive manufacturing of concentrated wound stator teeth, *Addit. Manuf. Lett.* 7 (July 2023) 100165, <https://doi.org/10.1016/j.addlet.2023.100165>.
- [29] S. Mao, D.Z. Zhang, Z. Ren, G. Fu, X. Ma, Effects of process parameters on interfacial characterization and mechanical properties of 316L/CuCrZr functionally graded material by selective laser melting, *J. Alloys Compd.* 899 (2022) 163256, <https://doi.org/10.1016/j.jallcom.2021.163256>.
- [30] C. Martendal, P. Esteves, L. Deillon, F. Malamud, A. Jamili, J. Löffler, M. Bam-bach, Effects of beam shaping on copper-steel interfaces in multi-material laser beam powder bed fusion, *J. Mater. Process. Technol.* 327 (2024) 118344, <https://doi.org/10.1016/J.JMATPROTEC.2024.118344>.
- [31] Z.H. Liu, D.Q. Zhang, S.L. Sing, C.K. Chua, L.E. Loh, Interfacial characterization of SLM parts in multi-material processing: metallurgical diffusion between 316L stainless steel and C18400 copper alloy, *Mater. Charact.* 94 (2014) 116–125, <https://doi.org/10.1016/j.matchar.2014.05.001>.
- [32] J. Chen, Y. Yang, C. Song, D. Wang, S. Wu, M. Zhang, Influence mechanism of process parameters on the interfacial characterization of selective laser melting 316L/CuSn10, *Mater. Sci. Eng. A* 792 (January 2020) 139316, <https://doi.org/10.1016/j.msea.2020.139316>.
- [33] K. Chen, C. Wang, Q. Hong, S. Wen, Y. Zhou, C. Yan, Y. Shi, Selective laser melting 316L/CuSn10 multi-materials: processing optimization, interfacial characterization and mechanical property, *J. Mater. Process. Technol.* 283 (March 2020) 116701, <https://doi.org/10.1016/j.jmatprotec.2020.116701>.
- [34] D. Wang, G. Wei Deng, Y. Qiang Yang, J. Chen, W. Hui Wu, H. Liang Wang, C. Lin Tan, Interface microstructure and mechanical properties of selective laser melted multilayer functionally graded materials, *J. Cent. South Univ.* 28 (4) (2021) 1155–1169, <https://doi.org/10.1007/s11771-021-4687-9>.
- [35] X. Wang, Z. Liu, Y. Tao, Y. Zhou, S. Wen, Y. Shi, Enhancing the interface strength of additively manufactured 316 L/CuSn10 bimetallic components through heterogeneous microstructures, *Addit. Manuf.* 78 (October 2023), <https://doi.org/10.1016/j.addma.2023.103860>.
- [36] Y. Bai, J. Zhang, C. Zhao, C. Li, H. Wang, Dual interfacial characterization and property in multi-material selective laser melting of 316L stainless steel and C52400 copper alloy, *Mater. Charact.* 167 (April 2020) 110489, <https://doi.org/10.1016/j.matchar.2020.110489>.
- [37] C. Tan, Y. Chew, G. Bi, D. Wang, W. Ma, Y. Yang, K. Zhou, Additive manufacturing of steel–copper functionally graded material with ultrahigh bonding strength, *J. Mater. Sci. Technol.* 72 (2021) 217–222, <https://doi.org/10.1016/j.jmst.2020.07.044>.
- [38] R.P. Shi, C.P. Wang, D. Wheeler, X.J. Liu, Y. Wang, Formation mechanisms of self-organized core / shell and core / shell / corona microstructures in liquid droplets of immiscible alloys, *Acta Mater.* 61 (4) (2013) 1229–1243, <https://doi.org/10.1016/j.actamat.2012.10.033>.
- [39] Z.A. Young, Q. Guo, N.D. Parab, C. Zhao, M. Qu, L.I. Escano, K. Fezzaa, W. Everhart, T. Sun, L. Chen, Types of spatter and their features and formation mechanisms in laser powder bed fusion additive manufacturing process, *Addit. Manuf.* 36 (July 2020) 101438, <https://doi.org/10.1016/j.addma.2020.101438>.
- [40] S. Ozawa, K. Morohoshi, T. Hibiya, Influence of oxygen partial pressure on surface tension of Molten type 304 and 316 stainless steels measured by oscillating droplet method using electromagnetic levitation, *ISIJ Int.* 54 (9) (2014) 2097–2103, <https://doi.org/10.2355/ISIJINTERNATIONAL.54.2097>.
- [41] W. Gale, T. Totemeier (Eds.), *Smithells Metals Reference Book, 8th edition, Butterworth-Heinemann, 2004*.
- [42] S.D. Jadhav, S. Dadbakhsh, L. Goossens, J.P. Kruth, J. Van Humbeeck, K. Van-meensel, Influence of selective laser melting process parameters on texture evolution in pure copper, *J. Mater. Process. Technol.* 270 (February 2019) 47–58, <https://doi.org/10.1016/j.jmatprotec.2019.02.022>.
- [43] A. Munitz, A. Venkert, P. Landau, M.J. Kaufman, R. Abbaschian, Microstructure and phase selection in supercooled copper alloys exhibiting metastable liquid miscibility gaps, *J. Mater. Sci.* 47 (23) (2012) 7955–7970, <https://doi.org/10.1007/S10853-012-6354-X/FIGURES/20>, <https://link.springer.com/article/10.1007/s10853-012-6354-x>.
- [44] D.E.J. Armstrong, A.J. Wilkinson, S.G. Roberts, Measuring anisotropy in Young's modulus of copper using microcantilever testing, *J. Mater. Res.* 24 (11) (2009) 3268–3276, <https://doi.org/10.1557/JMR.2009.0396/METRICS>, <https://link.springer.com/article/10.1557/jmr.2009.0396>.